materials

MDPI

Article

Adsorption and Visible Photocatalytic Synergistic Removal of a Cationic Dye with the Composite Material $BiVO_4$/MgAl–LDHs

Yuquan Wang [1,2], Yidong Xu [2], Xinjie Cai [1,2] and Jinting Wu [2,*]

[1] College of Civil Engineering and Architecture, Zhejiang University, Hangzhou 310058, China
[2] College of Civil Engineering and Architecture, NingboTech University, Ningbo 315100, China
* Correspondence: wujinting0215@nit.zju.edu.cn

Abstract: Adsorption and photocatalysis are effective in removing organic pollutants from wastewater. This study is based on the memory effects of MgAl–layered double hydroxides (MgAl–LDHs) after high-temperature calcination. By introducing bismuth vanadate ($BiVO_4$) during the reformation of the layered structure via contact with water, a composite material $BiVO_4$/MgAl–LDHs with enhanced adsorption and visible light catalytic performance was synthesized. The effects of the calcination temperature, ratio, initial methylene blue (MB) concentration, and catalyst dosage on the adsorption and photocatalytic performance were investigated. The $BiVO_4$/MgAl–LDHs showed better photocatalytic performance than the pure $BiVO_4$ and MgAl–LDHs. Under the optimal conditions, the proportion of MB adsorbed in 20 min was 66.1%, and the percentage of MB degraded during 100 min of photolysis was 92.4%. The composite photocatalyst showed good chemical stability and cyclability, and the adsorption-degradation rate was 86% after four cycles. Analyses of the adsorption and photocatalytic mechanisms for the composite material showed that synergistic adsorption and visible light photocatalysis contributed to the excellent catalytic performance of the $BiVO_4$/MgAl–LDHs. A highly adsorbent photocatalytic composite material exhibiting outstanding performance was prepared via a simple, cost-effective, and environmentally friendly method, providing reference information for the removal of organic pollutants from liquids.

Keywords: $BiVO_4$; MgAl–LDHs; memory effect; adsorption-visible photocatalytic performance; organic pollutants

check for updates

Citation: Wang, Y.; Xu, Y.; Cai, X.; Wu, J. Adsorption and Visible Photocatalytic Synergistic Removal of a Cationic Dye with the Composite Material $BiVO_4$/MgAl–LDHs. *Materials* **2023**, *16*, 6879. https://doi.org/10.3390/ma16216879

Received: 1 September 2023
Revised: 17 October 2023
Accepted: 20 October 2023
Published: 26 October 2023

Copyright: © 2023 by the authors. Licensee MDPI, Basel, Switzerland. This article is an open access article distributed under the terms and conditions of the Creative Commons Attribution (CC BY) license (https://creativecommons.org/licenses/by/4.0/).

1. Introduction

With the acceleration of urbanization and industrialization, the material living standards of people have continuously improved; however, urbanization and industrialization severely challenge the environment. Among instances of these processes, the discharge of dye wastewater with high toxicity, high chroma, and complex composition seriously threatens the ecological environment and human health [1,2]. In the past ten years, researchers have attempted to use multiple techniques, including biological methods, physical/chemical adsorption, and Fenton processes [3] to treat sewage; nevertheless, these traditional treatment methods cannot be widely applied due to their disadvantages, including their high cost, complexity, and poor organic-pollutant-selectivity [4]. Due to its mild reaction conditions, high degradation efficiency, and ability to avoid secondary pollution, semiconductor photocatalytic technology has played a vital role in solar energy conversion and environmental protection measures [5]. As one of the first widely used photocatalysts, TiO_2 has the advantages of nontoxicity, low cost, high chemical stability, strong oxidative reduction, and abundant natural reserves [6–9]. However, TiO_2 can only respond to ultraviolet light because of its large band gap (3.2 eV), and its sunlight utilization rate is low [10]. In addition, the photocatalytic performance of TiO_2 is reduced due to the rapid recombination of photogenerated carriers [11], limiting its real-world applicability.

To overcome these shortcomings, improving the conversion of solar energy and the degradation rate of pollutants has become the focus of research in the field of photocatalysis. Notably, the proportion of ultraviolet light in sunlight is only 4–6%, while the proportion of visible light can reach 45% [8]. Therefore, the successful design of photocatalysts that can respond to visible light is becoming a popular subject among researchers.

Recent studies have confirmed that among many visible–light–metal–oxide–photocatalysts, bismuth vanadate ($BiVO_4$) is a highly promising visible light catalyst [12]. The high abundance and narrow bandgap (approximately 2.4 eV) of $BiVO_4$ make it vital for the photocatalytic degradation of organic matter [13,14]. However, the narrow bandgap facilitates recombination of the photogenerated electrons and holes [15]. Add–tionally, the low specific surface area of the pore–free structure and low light absorption also inhibit the photocatalytic reactions [16]. To enhance the light absorption efficiency and suppress the recombination of photogenerated electrons and holes, modifications of $BiVO_4$ with other materials have attracted considerable attention [17–19]. Among the modification methods, the construction of heterojunctions is considered the most effective [20]. Although the heterojunctions effectively mitigate recombination of the photogenerated charge carriers, the adsorptivities of the photocatalytic composite materials are not high. Moreover, they do not exhibit efficient photocatalysis with insufficient light or in the dark, thus limiting the effective removal of organic pollutants. However, studies have shown that [21,22] composite photocatalytic materials formed by combining Bi–VO_4 with strongly adsorptive materials can overcome the challenges of unfavorable environmental conditions and realize efficient removal of organic pollutants.

Layered double hydroxides (LDHs), also known as hydrotalcites, have the general formula $[M_{1-x}^{2+}\ M_x^{3+}\ (OH)_2]\ [Ax_{/n}]^{n-}\cdot mH_2O$, where M^{2+}, M^{3+}, and A^{n-} represent divalent cations, trivalent cations, and interlayer anions [23]. The unique structures of LDHs are formed by electrostatic interactions between positively charged brucite-like octahedra and interlayer anions [24]. Due to their stable layered structures, large specific surface areas, strong adsorption capacities, and tunable band gaps, LDHs have attracted significant attention in photocatalysis [25–27]; they are ideal photocatalysts [28], catalyst supports [29], and adsorbents [16]. As photocatalysts, LDHs doped with transition metal elements are high-performance heterogeneous materials [28,30]. Furthermore, the LDHs can serve as both carriers and co-catalysts. When metals, metal oxides, or non-metal materials are dispersed within the LDH layered structure, a synergistic effect between the two materials can be achieved [31]. Additionally, when combined with other semiconductor materials, the MgAl–layered double hydroxide (MgAl–LDH) particles can serve as a barrier layer for electrons and capture site recombination, leading to improved spatial charge separation [32]. Yang et al. [33] found that materials like activated carbon, bentonite, and fly ash have low adsorption capacities and are difficult to recycle, whereas LDHs exhibit strong adsorption and provide photocatalytic degradation of adsorbed organic pollutants, allowing for repeated use of the adsorbents. In addition to the aforementioned characteristics, the memory effect is also a significant feature of LDHs. Research has revealed that LDHs subjected to high-temperature calcination (LDO) exhibit a memory effect. When exposed to water, they reconstruct their parent structure through layer-by-layer rebuilding [34], which generates oxygen and metal vacancy defects in the parent structure [35]. The creation of defects reduces the band gap, expands the light absorption range, and separates the photogenerated charge carriers. This study was based on the distinctive memory effect, strong adsorption performance, and exceptional catalytic activity of MgAl–LDHs. The introduction of $BiVO_4$ when MgAl–LDO was treated with water triggered a laminate reconstruction process, leading to the synthesis of a composite material, $BiVO_4$/MgAl–LDHs, which exhibited strong adsorption and efficient visible light catalysis.

In this paper, we used MgAl–LDHs and $BiVO_4$ as raw materials to prepare a highly adsorbent photocatalytic composite material, $BiVO_4$/MgAl–LDHs; we studied its adsorption capacity and photocatalytic degradation of methylene blue (MB) while considering the effects of multiple factors, including the calcination temperature, ratio, initial MB con-

centration, and catalyst dosage, on photocatalytic performance. Second, X-ray dif–fraction (XRD), X-ray photoelectron spectroscopy (XPS), scanning electron microscopy (SEM), transmission electron microscopy (TEM), Brunauer-Emmett-Teller (BET), and high-resolution transmission electron microscopy (HRTEM) were used to determine the morphology, crystal structure, and chemical binding state of the photocatalyst. Various techniques, including XPS valence band analysis, ultraviolet-visible (UV–vis) spectroscopy, and photoluminescence (PL) spectroscopy, were used to determine the energy band positions and optical properties of the catalyst. Finally, we analyzed the adsorption mechanism and the photocatalytic mechanism of the $BiVO_4$/MgAl–LDH composite material.

2. Materials and Methods

2.1. Materials

MgAl–LDHs and isopropanol (IPA) were purchased from Guangdong Wengjiang Chemical Reagent Co., Ltd. (Shaoguan, China). $BiVO_4$ was purchased from the Shanghai Dingyun Reagent Business Department. A total of 1–4 pairs of benzoquinone (BQ) were purchased from Shanghai Aladdin Biochemical Technology Co., Ltd. (Shanghai, China). Disodium ethylenediaminetetraacetic acid (EDTA–2Na) was purchased from Shanghai Zhanyun Chemical Co., Ltd. (Shanghai, China). The MB indicator was purchased from Wuxi Yatai United Chemical Co., Ltd. (Wuxi, China). The chemical reagents and materials used in this study were not further purified, and the water used in the experiments was deionized.

2.2. Synthesis of Photocatalyst $BiVO_4$/MgAl–LDHs

The synthesis of the $BiVO_4$/MgAl–LDHs composite photocatalytic material mainly included the following steps (as shown in Figure 1). First, 60 g of MgAl–LDH powder was weighed and placed in a crucible. Then, the crucible was placed in the center of a muffle furnace for roasting. To explore the influences of roasting temperature, the firing temperature was set to 300 °C, 400 °C, 500 °C, and 600 °C, and the temperature was kept constant for 5 h. After the specified time, the muffle furnace was opened. After cooling to room temperature, the roasted MgAl–LDHs (MgAl–LDO) were removed. The MgAl-LDO samples prepared at various temperatures are illustrated in Figure 2. A total of 200 mL of deionized water was poured into a 1000 mL beaker. To explore the influences of different pure material ratios, $BiVO_4$ and MgAl–LDO were mixed according to 2:8 (20% $BiVO_4$/MgAl–LDHs), 3:7 (30% $BiVO_4$/MgAl–LDHs), and 5:5 (50% $BiVO_4$/MgAl–LDHs) ratios; additionally, 400 mg, 600 mg, and 1000 mg of $BiVO_4$ and 1600 mg, 1400 mg, and 1000 mg of MgAl–LDO were weighed for the material ratios of 2:8, 3:7, and 5:5, respectively. Each of the above groups of $BiVO_4$ and MgAl–LDO was added to a beaker containing deionized water, placed on a magnetic stirrer and stirred for 6 h. Then, the beaker was placed in a drying oven at 105 °C for drying, and the beaker was removed to cool after the drying was completed. After reaching room temperature, the sample in the beaker was ground into a powder with agate powder and sieved with a 100-mesh sieve to obtain the composite photocatalytic material $BiVO_4$/MgAl–LDHs used in this study.

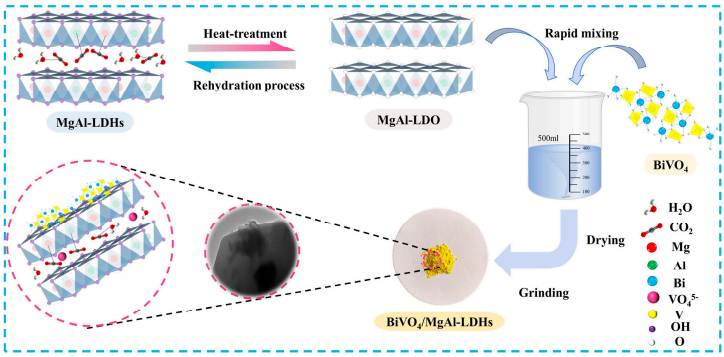

Figure 1. Schematic diagram showing the synthesis of $BiVO_4$/MgAl–LDHs.

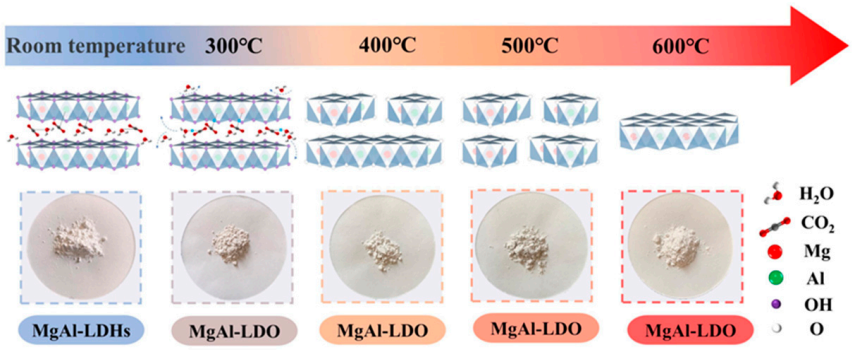

Figure 2. Calcination products of the MgAl–LDHs formed at different temperatures.

2.3. Characterization

The morphologies and structures of the photocatalysts were observed and analysed using SEM (Tescan Mira4, Energy spectrum: xplore, TESCAN Brno, s.r.o., Brno, Czech Republic) and TEM (tecnai F20, FEI Corporation, Hillsboro, OR, USA). XRD (D8 Advance, AXS Corporation, Brooke, Germany) was used to detect the material com–positions and crystal structures of the samples. UV–Vis diffuse reflection spectroscopy (Shimadzu 3600-plus, Shimadzu Corporation, Kyoto, Japan) was used to analyze the op–tical properties of the materials. Fourier transform infrared absorption spectroscopy (FTIR; Thermo Nicolet iS5, Waltham, MA, USA), XPS (American Thermo Fisher Scientific K-Alpha, Waltham, MA, USA), and steady-state/transient PL spectroscopy (Edinburgh FLS-1000, Edinburgh Instruments UK, Edinburgh, UK) were used to investigate the functional group types, surface chemical properties, and electron–hole pair recombination characteristics. The best com–posite photocatalytic material was 30% $BiVO_4$/MgAl-LDH calcined at 300 °C.

2.4. Adsorption-Photocatalytic Degradation Experiments with MB

First, 100 mL of a 10 mg/L MB solution was prepared and poured into a beaker equipped with a stirrer. At that time, approximately 6 mL of the initial MB solution (C_0) was extracted and filtered into a centrifuge tube. Subsequently, 500 mg of the composite material $BiVO_4$/MgAl–LDHs was weighed and added to the beaker containing the MB solution. All light sources were turned off simultaneously. The beaker was then transferred to a magnetic stirrer, and the stirring speed was maintained at 270 r/min for 20 min. After stirring was completed, the photocatalytic material and MB reached adsorp–tion–desorption equilibrium. Simultaneously, about 6 mL of the MB solution (C_1) was ex–tracted and filtered into a centrifuge tube. The light source was a 300 W xenon lamp with a 400 nm filter. The distance between the light source and the liquid surface was 45 cm, and the xenon lamp was turned on 10 min in advance for preheating. After the visible light catalytic reaction started, samples were drawn every 20 min, and the experiment ended after 100 min of light irradiation. Finally, the obtained samples were centrifuged (6000 r/min for 5 min), and the absorbance of the MB solution at different time points was measured with a 756S UV-visible spectrophotometer. Based on the relation–ship between absorbance and concentration, the concentration of the MB solution was determined at each time point.

The adsorption efficiency (R) and photocatalytic degradation rate (η_t) for MB were calculated with Equations (1) and (2), respectively:

$$R = (C_0 - C_1)/C_0 \times 100\% \quad (1)$$

$$\eta_t = (C_1 - C_t)/C_1 \times 100\% \quad (2)$$

$$\text{Adsorption-degradation rate} = (C_0 - C_t)/C_0 \times 100\% \quad (3)$$

where C_0 ($mg \cdot L^{-1}$) is the initial concentration of the methylene blue solution, R(%) is the MB adsorption efficiency during the dark adsorption stage, C_1 ($mg \cdot L^{-1}$) is the initial con–centration of the MB solution at the start of illumination, C_t ($mg \cdot L^{-1}$) is the concentration

of MB solution at time t (min) during illumination, and η_t(%) is the photocatalytic degradation rate at time t.

3. Results and Discussion

3.1. Characterization of Photocatalysts

3.1.1. XRD and FTIR Analysis

In Figure 3a, the XRD patterns of $BiVO_4$, MgAl–LDHs, and $BiVO_4$/MgAl–LDHs show that all of the diffraction peaks of pure $BiVO_4$ are consistent with the $BiVO_4$ monoclinic phase (PDF #14-0688) [36,37]. The diffraction peaks for the MgAl–LDHs exhibited high intensities and indicated distinct separation of the crystal planes, suggesting high crystallinity and regularity between the layers [38]. All of the diffraction peaks in the $BiVO_4$/MgAl–LDHs XRD pattern are composed of $BiVO_4$ and MgAl–LDHs; MgAl–LDHs have more diffraction peaks than $BiVO_4$, which may be related to the higher proportion of MgAl–LDHs than $BiVO_4$ during material synthesis. The diffraction peaks after re–combination still maintain the characteristics of the two pure materials, suggesting that the $BiVO_4$/LDHs were prepared successfully.

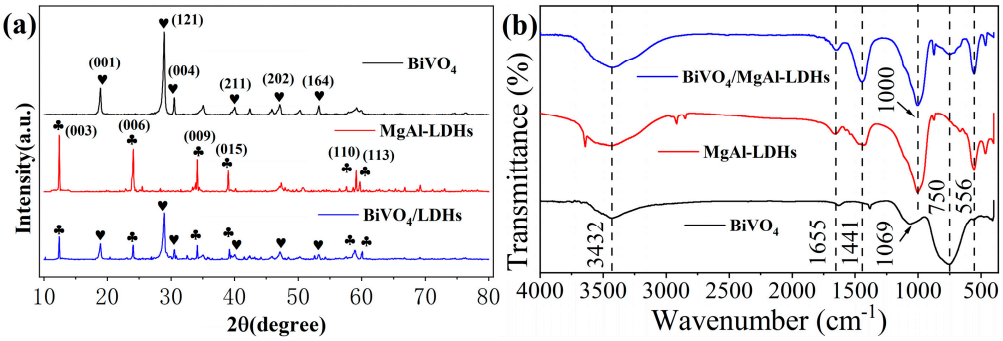

Figure 3. XRD patterns for $BiVO_4$, MgAl–LDHs and $BiVO_4$/ MgAl–LDHs (**a**) and FTIR spectra of $BiVO_4$/ MgAl–LDHs, MgAl–LDHs and $BiVO_4$ (**b**).

In the FTIR spectra (Figure 3b), the peaks centered at approximately 1655 cm^{-1} and 3432 cm^{-1} of $BiVO_4$ are mainly attributed to the bending and stretching vibrations of the adsorbed water molecules [39]; the peaks at 750 cm^{-1} and 1069 cm^{-1} are related to the bending vibration of VO_4^{-3} [40] and the asymmetric tensile vibration of V–O [41], respectively. The strong and wide peak at 3432 cm^{-1} in MgAl–LDHs arises mainly due to the stretching vibrations of OH in the Mg $(OH)_2$ layer, Al $(OH)_3$ layer, and interlayer H_2O. The peaks at 1655 cm^{-1}, 1441 cm^{-1}, and 1000 cm^{-1} originate from the bending vibrations of water molecules, the ν_3 vibration mode of CO_3^{2},' and the translational motion of OH, respectively. The peaks near 556 cm^{-1} are interpreted as M–OH bending and M–O tensile vibration in the octahedral main layer [42]. In addition, the FTIR spectra of the composite material $BiVO_4$/MgAl–LDHs exhibit the spectral characteristics of both $BiVO_4$ and MgAl–LDHs, further indicating the successful preparation of the composite $BiVO_4$/MgAl–LDHs.

3.1.2. SEM, TEM and Energy-Dispersive X-ray Spectroscopy (EDS) Analyses

The morphologies and microstructures of $BiVO_4$, MgAl–LDHs, and $BiVO_4$/MgAl–LDHs were studied by TEM. As shown in Figure 4, $BiVO_4$ has an irregular block structure formed by the aggregation of particles [43] (Figure 4a) and MgAl–LDHs are hexagonal plates with certain thicknesses and surface sizes of approximately 2 μm [44] (Figure 4b). The composite material $BiVO_4$/MgAl–LDHs retains the main structure of pure $BiVO_4$ and MgAl–LDHs and tightly attaches $BiVO_4$ to the surfaces of the hexagonal plates of MgAl–LDHs (Figure 4c,d). As shown in Figure 4e–g, the crystal plane distributions in the HRTEM images confirm the coexistence of $BiVO_4$ and MgAl–LDHs, where the crys–tal plane fringe spacings of 0.317 nm and 0.242 nm correspond to the crystal plane of MgAl–

LDHs and the crystal plane of $BiVO_4$, respectively. The tight connection formed between these two semiconductor materials facilitates charge transfer [45]. Figure 4h shows that the distribution of $BiVO_4$ in area ② is more uniform than that in area ①, in–dicating that LDHs can somewhat reduce the occurrence of $BiVO_4$ agglomeration and deactivation, thereby exposing an increased number of active centers. Elemental map–ping of $BiVO_4$/MgAl–LDHs shows that vanadium, oxygen, bismuth, magnesium, and aluminum are evenly distributed on the surface of the photocatalyst, indicating that the heterojunction interface formed between $BiVO_4$ and MgAl–LDHs is close (Figure 4i–m); Wang et al. derived similar conclusions [46]. Figure 4n shows the relationship between the elemental content of each component in $BiVO_4$/MgAl–LDHs, in which the contents of oxygen and aluminum are relatively high, and the contents of bismuth and magnesi–um are relatively low.

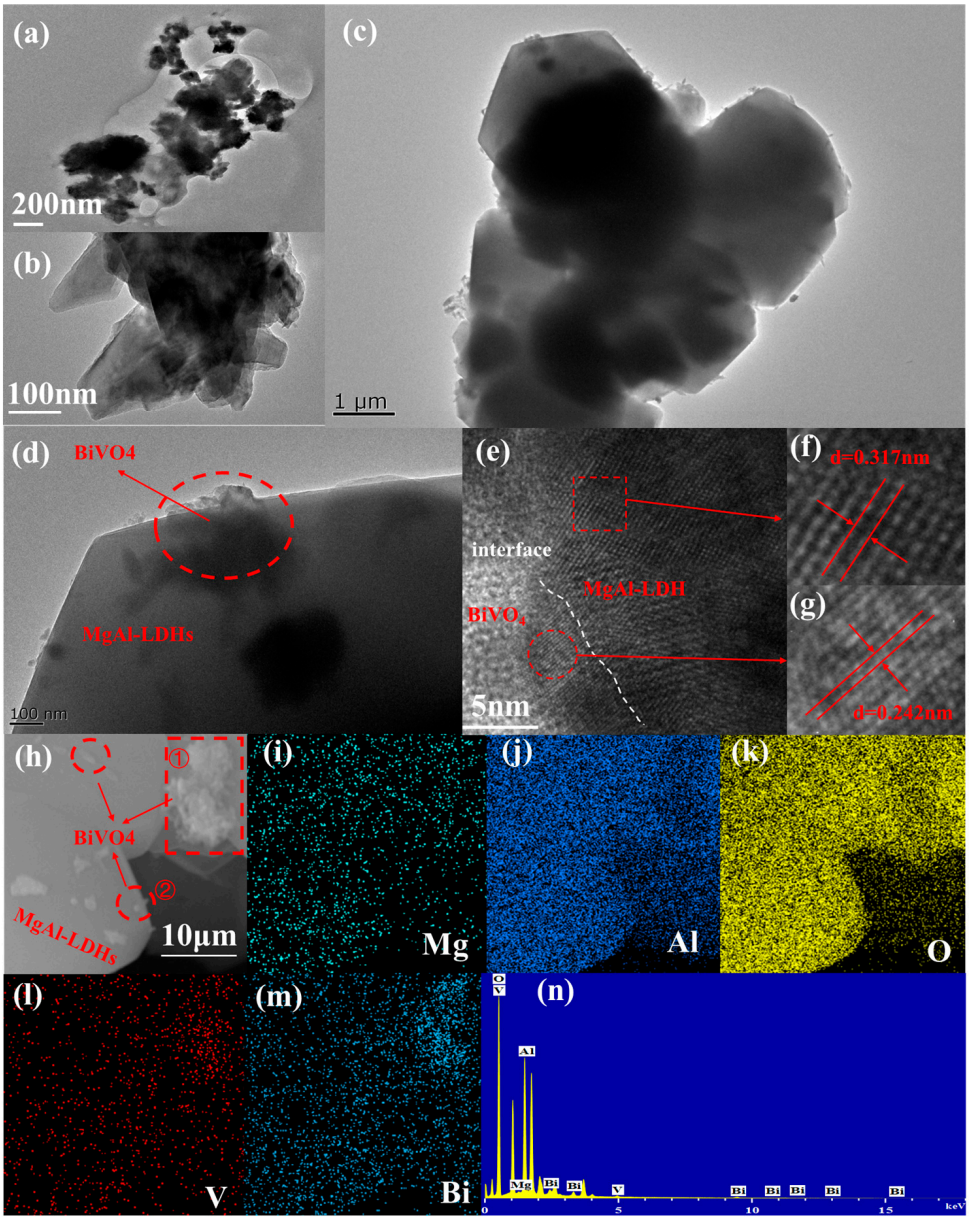

Figure 4. TEM images of $BiVO_4$ (**a**), MgAl–LDHs (**b**), and $BiVO_4$/MgAl–LDHs (**c**,**d**); HRTEM images of $BiVO_4$/MgAl–LDHs (**e**–**g**); SEM–EDS elemental mapping images of $BiVO_4$/MgAl–LDHs (**h**–**m**); and EDS spectrum of $BiVO_4$/MgAl–LDHs (**n**).

3.1.3. BET Analyses

The BET surface areas (A_{BET}) and pore volumes of $BiVO_4$ and $BiVO_4$/MgAl–LDHs were evaluated with N_2 adsorption–desorption isotherms [47], as depicted in Figure 5d. The isotherm for $BiVO_4$/MgAl–LDHs is classified as a Type V isotherm, and it exhibits a vague hysteresis loop when the P/P_0 range is between 0.7 and 1.0. On the other hand, the isotherm for $BiVO_4$ is identified as a Type II isotherm, indicating that $BiVO_4$ is a non-porous material. As shown in Table 1, compared to pure $BiVO_4$, the composite material $BiVO_4$/MgAl–LDHs displays significantly higher A_{BET}, V_{BJH}, and D_{BJH} values, indicating a noticeable structural alteration upon the incorporation of the MgAl–LDH. This alteration primarily stems from the inhibited aggregation of the $BiVO_4$ particles after they were loaded onto the high specific-surface-area and porous MgAl–LDHs, as highlighted in Figure 4h.

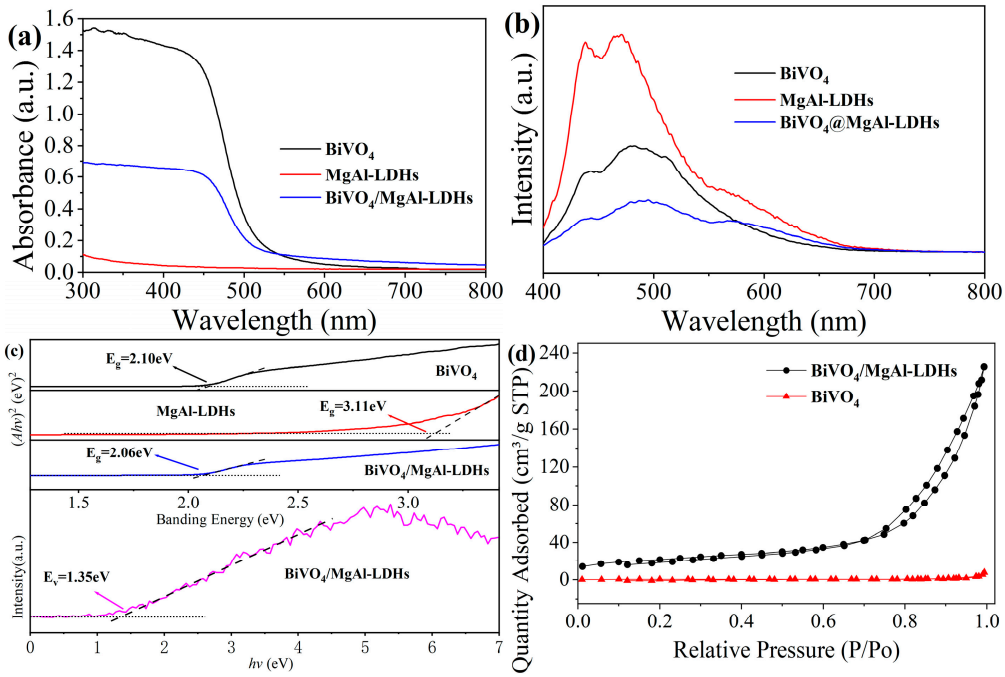

Figure 5. UV–vis diffuse reflectance spectra of $BiVO_4$, MgAl–LDHs and $BiVO_4$/MgAl–LDHs (**a**); photoluminescence spectra of $BiVO_4$, MgAl–LDHs and $BiVO_4$/MgAl–LDHs excited at 260 nm (**b**); optical band gaps of $BiVO_4$, MgAl–LDHs and $BiVO_4$ (**c**); Nitrogen sorption isotherms for $BiVO_4$ and the $BiVO_4$/MgAl–LDHs (**d**).

Table 1. BET surface areas (ABET), pore volumes (VBJH), and pore diameters (DBJH) for $BiVO_4$ and $BiVO_4$/MgAl-LDHs.

Sample	ABET (m^2/g)	VBJH (cm^3/g)	DBJH (nm)
$BiVO_4$	2.57 m^2/g	0.01 cm^3/g	14.99 nm
$BiVO_4$/MgAl–LDHs	76.52 m^2/g	0.35 cm^3/g	16.27 nm

3.1.4. PL, UV–Vis–NIR Analysis

Figure 5a shows the ultraviolet–visible absorption spectra of the three samples. The composite material $BiVO_4$/MgAl–LDHs has a higher absorbance than $BiVO_4$ in the visible region < 542 nm and the absorbance of $BiVO_4$/MgAl–LDHs is lower than that of $BiVO_4$ when the wavelength is >542 nm. However, the absorbance of MgAl–LDHs is very low throughout the visible light region, further indicating that it does not respond to visible light. By taking hv as the abscissa and $(Ahv)^2$ as the ordinate for plotting (Figure 5c), we find that the band gap widths of $BiVO_4$/MgAl–LDHs and $BiVO_4$ can be obtained as 2.09 eV and 2.05 eV, respectively. Therefore, compounding MgAl–LDHs can tune the forbidden band width of pure $BiVO_4$, thereby expanding its visible light response range.

PL spectroscopy can be used to characterize the separation and transfer characteristics of photogenerated electron–hole pairs; the higher the luminescence intensity is, the higher the degree of recombination of photogenerated carriers. As shown in Figure 5b, all three materials have intensity peaks near 473 nm, among which MgAl–LDHs have the highest intensity peak, and $BiVO_4$/MgAl–LDHs have the lowest intensity peak. The results show that the composite photocatalytic material $BiVO_4$/MgAl–LDHs has a higher separation efficiency of photogenerated carriers than the pure materials $BiVO_4$ and MgAl–LDHs. This phenomenon may arise because the positive surface charges of MgAl–LDHs capture the photogenerated electrons in $BiVO_4$, thereby prolonging the lifetime of photogenerated carriers. In addition, the difference in the Fermi energy level between $BiVO_4$ and MgAl–LDHs may reduce the recombination rates of photogenerated electrons and holes [48].

3.1.5. XPS Analysis

XPS of $BiVO_4$, MgAl–LDHs, and $BiVO_4$/MgAl–LDHs was used to explore the changes in the elemental compositions and states of the sample surfaces after recombination. As shown in Figure 6a, the composite material $BiVO_4$/MgAl–LDHs are mainly composed of five elements, Mg, Al, Bi, V, and O, and the contents of Mg and Bi are relatively small; this trend is consistent with the results of Figure 4n, further determining the elemental compositions of the composite $BiVO_4$/MgAl–LDHs. By taking the peak at C 1s 284.8 eV as the reference standard (Figure 6c) [49], we find two sets of characteristic peaks at 531.64 eV and 533.65 eV (Figure 6d); the peak at 531.64 eV is mainly attributed to the metal oxide oxygen in the group [50], and the peak at 533.65 eV may be related to C–O–C and O–C=O in MgAl–LDHs [51]. In the XPS images of pure $BiVO_4$ V 2p (Figure 6b), the two peaks at 524.23 eV and 516.73 eV belong to V $2p_{1/2}$ and V $2p_{3/2}$, respectively [52]. Compared with pure $BiVO_4$, in the composite material $BiVO_4$/MgAl–LDHs, the peak intensities of both V $2p_{1/2}$ and V $2p_{3/2}$ decrease, mainly because the greatly reduced low-valent V participates in the redox reaction and is consumed during composite synthesis. Second, the peaks at V $2p_{1/2}$ and V $2p_{3/2}$ move forward to 524.6 eV and 517.09 eV, respectively. The two peaks at 158.92 eV and 164.24 eV in Figure 6e represent Bi $4f_{5/2}$ and Bi $4f_{7/2}$, respectively, indicating that the ion form of Bi in the composite photocatalyst is Bi^{3+} [53]. Compared with pure $BiVO_4$, Bi $4f_{5/2}$ and Bi $4f_{7/2}$ in $BiVO_4$/MgAl–LDHs move in the direction of high binding energy. Here, the electron binding energies are 159.08 eV and 164.33 eV for Bi $4f_{5/2}$ and Bi $4f_{7/2}$, respectively. The above positive movement phenomenon may occur due to the deposition of $BiVO_4$ on MgAl–LDHs. This deposition changes the local chemical environment so that $BiVO_4$ can act as an acceptor to receive photogenerated electrons transferred from MgAl–LDHs; related studies have resulted in similar conclusions [54,55]. Contrary to the direction of movement of the abovementioned orbital electron binding energy, unlike pure MgAl–LDHs, the electron binding energy at Al 2p in $BiVO_4$/MgAl–LDHs moves inversely from 74.15 to 74.13 eV (Figure 6f), which may be related to the newly formed unstable bond in the composite [56].

3.2. Photocatalytic Degradation of the MB Solution under Visible Light

3.2.1. Effect of Firing Temperature

To explore the effect of the calcination temperature of MgAl–LDHs on the adsorption of visible light and catalytic removal of MB, the products of the MgAl–LDHs were calcined at 300 °C, 400 °C, 500 °C, and 600 °C (MgAl–LDO), and a composite with $BiVO_4$ was synthesized. The synthetic steps of the composite visible light catalytic materials are shown in Figure 1. The photocatalytic capabilities of these four composite materials were evaluated under identical conditions, and the results are illustrated in Figure 7a. At calcination temperatures between 300 °C and 500 °C, the adsorption efficiencies of the composite materials remain around 75%. However, as the calcination temperature increases to 600 °C, the adsorption efficiencies of the composite materials decrease to 34.6%. These substantial drops in the adsorption efficiencies are primarily attributed to the collapse and disruption of the core layered structures of the calcination products, resulting in

the formation of a spinel structure with a smaller specific surface area and pore volume. Secondly, the degradation rates of the blank control group and the 300 °C, 400 °C, 500 °C, and 600 °C calcination groups are 23%, 92.4%, 86.8%, 75.0%, and 59.0%, respectively. The four composite materials show better photocatalytic performance than the control group, among which the photocatalytic effects at a calcination temperature of 300 °C are the best and at a calcination temperature of 600 °C are the poorest. This phenomenon occurs mainly because as the calcination temperature increases, the morphologies and crystal structures of the calcination products change to varying degrees. When the calcination temperature increases to 300 °C, MgAl–LDHs release H_2O and CO_2 successively. Based on the memory effect [57], MgAl–LDHs after calcination can still recover their layered structures in the presence of deionized water. We prepared BiVO4/MgAl–LDHs by combining MgAl–LDHs in layered reconstruction with BiVO4. When the calcination temperature increases from 300 °C to 400 °C and then to 500 °C, the MgAl–LDHs after calcination cannot recover their regular and orderly original layered structures, and their memory effects begin to weaken. Here, the degradation rate of the composite photocatalytic material begins to decrease. When the calcination temperature further increases to 600 °C, the main layered structures of the MgAl–LDHs are completely collapsed and destroyed, forming spinel structures with small specific surface areas and pore volumes; additionally, the memory effect is lost. Moreover, the degradation rate of the composite-formed photocatalytic material is the lowest. Second, when the calcination temperature is 250 °C [58] or lower [40], MgAl–LDHs lose interlayer water without significant structural changes, and their memory effects cannot be used to compound Bi–VO_4/MgAl–LDHs; therefore, the calcination temperature of MgAl–LDHs in this study is selected as 300 °C.

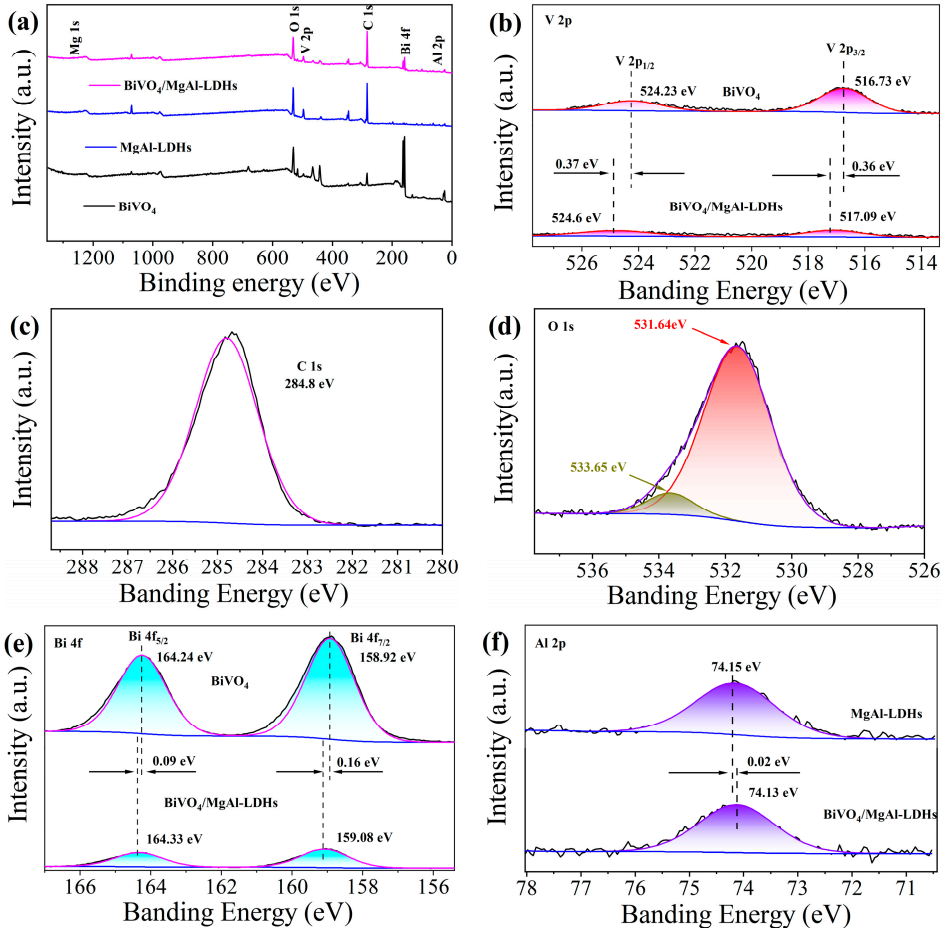

Figure 6. XPS survey spectra of $BiVO_4$/LDHs, MgAl–LDHs and $BiVO_4$ (**a**); XPS high–resolution spectra of V 2p (**b**), C 1s (**c**), O 1s (**d**), Bi 4f (**e**), and Al 2p (**f**).

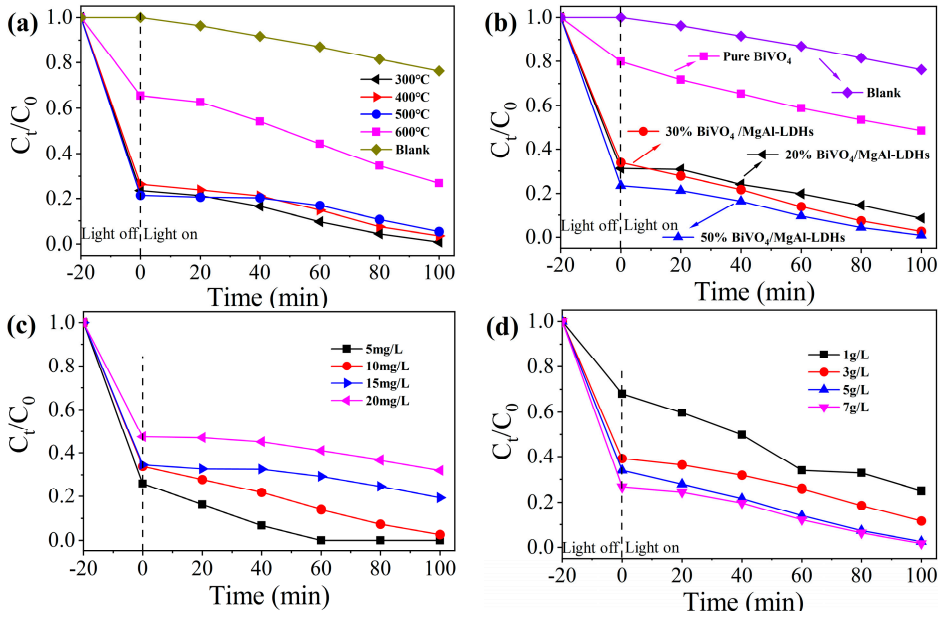

Figure 7. Relationship between the visible light catalytic degradation of MB and irradiation time under different calcination temperatures (**a**), ratios (**b**), initial dye concentrations (**c**), and photocatalyst concentrations (**d**).

3.2.2. Effect of the Material Ratio

Pure $BiVO_4$ easily causes accumulation and agglomeration inactivation, and the cost is overly high. An appropriate dosage of MgAl–LDHs can effectively improve the separation efficiencies of photogenerated carriers in $BiVO_4$ and reduce the production costs of composite materials. $BiVO_4$ and MgAl–LDHs were used to synthesize the composite materials 20% $BiVO_4$/MgAl–LDHs, 30% $BiVO_4$/MgAl–LDHs, and 50% $BiVO_4$/MgAl–LDHs with ratios of 2:8, 3:7, and 1:1, respectively. Since MgAl–LDHs (ecbm = −0.61 eV, evbm = 2.59 eV, Eg = 3.2 eV) do not respond to visible light, we must use a blank control group, pure $BiVO_4$, 20% $BiVO_4$/MgAl–LDHs, 30% $BiVO_4$/MgAl–LDHs, and 50% Bi–VO_4/MgAl–LDHs to investigate the effects of the material ratio on the adsorption and photocatalytic degradation of MB (Figure 7b). When the proportion of $BiVO_4$ is 20%, 30%, and 50%, the MB adsorption efficiencies during 20 min in the dark are approximately 70%. Compared to pure $BiVO_4$, there is a 50% increase in the adsorption efficiency. This is attributed to (i) improved dispersion of the $BiVO_4$, which exposed more active surfaces; (ii) the high specific surface area of the MgAl–LDHs provided more adsorption sites; and (iii) the interaction between $BiVO_4$ and MgAl–LDHs enhanced the microstructure and surface characteristics of the composite material, as shown in Figure 5b. The degradation rates of the blank control group, pure $BiVO_4$, 20% $BiVO_4$/MgAl–LDHs, 30% $BiVO_4$/MgAl–LDHs, and 50% $BiVO_4$/MgAl–LDHs test groups are 23.4%, 39.4%, 72.3%, 92.4%, and 96.6%, respectively. The results show that the incorporation of MgAl–LDHs can improve the photocatalytic performance of $BiVO_4$. As the proportion of $BiVO_4$ increases (20–50%), the photocatalytic performance of the composite material gradually improves; however, the increase in the degradation rate gradually decreases. The degradation rates of 30% $BiVO_4$/MgAl–LDHs and 50% $BiVO_4$/MgAl–LDHs are sufficiently high to nearly completely degrade the MB solution. The above results show that incor–porating an appropriate amount of MgAl–LDHs can effectively alleviate the agglomera–tion and deactivation of $BiVO_4$ and provide more active sites for the photocatalytic reaction. Second, considering the production cost of $BiVO_4$ and the photocatalytic effect of the composite material, we select $BiVO_4$ as the 30% composite photocatalytic material.

3.2.3. Effect of Initial MB Concentration

Different MB initial concentrations (5 mg/L, 10 mg/L, 15 mg/L, and 20 mg/L) and 500 mg of 30% $BiVO_4$/MgAl–LDHs were used to study the effects of the initial MB con–centration on the adsorption capacity and photocatalytic activity. The results are shown in Figure 7c. As the initial concentration of the MB solution increases from 5 mg/L to 20 mg/L, the adsorption efficiencies are 74.2%, 66.1%, 65.3%, and 52.5%, respectively. With increases in the initial MB concentration, the adsorption efficiency consistently decreases. This is primarily due to the fact that at higher initial MB concentrations, there are insufficient active adsorption sites on the surface of the composite material to adsorb all of the MB in the solution. The higher concentration of MB results in more unabsorbed MB, leading to a reduction in adsorption efficiency as the initial MB concentration was increased. The MB solution with a concentration of 5 mg/L is completely degraded when illuminated for 60 min, and the degradation rates corresponding to 10 mg/L, 15 mg/L, and 20 mg/L are 92.4%, 42.6%, and 32.5% when illuminated for 100 min, respectively. As the initial concentration of methylene blue increases, the photocatalytic degradation rate decreases continuously. This trend occurs mainly because low-concentration MB solutions can be completely degraded by sufficient active free radicals, while high-concentration MB solutions cannot be effectively decomposed and occupy a relatively high number of catalyst surface active sites, thus reducing the number of highly oxidative hydroxyl radicals [59]. Moreover, high-concentration MB solutions shorten the path lengths of photons penetrating the solution and prevent photons from reaching the surface of the photocatalyst [60]. In addition, an increasing number of sulfides, chlorides, and other intermediates adsorbed on the active site of the photocatalyst surface nega–tively impact photocatalytic degradation. To compare the photocatalytic degradation ef–fect over a long period with other experimental groups and ensure that the initial con–centration of the MB solution is not overly high, the initial concentration of MB solution selected in this study is 10 mg/L.

3.2.4. Effect of Photocatalyst Dosage

A 10 mg/L methylene blue solution was used with various 30% $BiVO_4$/MgAl–LDHs dosages (1 g/L, 3 g/L, 5 g/L, 7 g/L) to investigate the influence of the photocatalyst dos–age on both the adsorption capacity and photocatalytic activity. The results are shown in Figure 7d. When the catalyst dosage increases from 1 g/L to 7 g/L, the corresponding ad–sorption efficiencies are 32%, 60.8%, 66.1%, and 73.3%, respectively. The increased ad–sorption efficiencies are attributed to the greater availability of active adsorption sites [61]. Secondly, when the amount of catalyst increases from 1 g/L to 3 g/L, 5 g/L, and 7 g/L, the corresponding degradation rates are 63.3%, 70.4%, 92.4%, and 93.5%, respectively; additionally, the photocatalytic degradation rate continues to increase. The degrada–tion rate does not increase significantly when the catalyst dosage increases from 5 g/L to 7 g/L. This phenomenon occurs mainly because with the increase in the amount of pho–tocatalyst, more photogenerated electron–hole pairs and free radicals are generated and more active sites are exposed, thus improving the photocatalytic degradation efficiency [62]. However, when the amount of catalyst increases to a certain amount, the suspend–ed catalyst particles block a part of the incident light, thereby reducing the photon effi–ciency. Here, the degradation rate no longer increases or shows a downward trend [60,63]. A reasonable amount of photocatalyst is crucial for photocatalytic degradation experiments. When the amount of photocatalyst exceeds 5 g/L, the amount of photocata–lyst is no longer the main factor affecting its degradation rate; therefore, the optimal amount of photocatalyst selected in this study is 5 g/L.

3.2.5. Reaction Kinetics Analysis

To investigate the effects of the calcination temperature, material ratio, initial MB concentration, and photocatalyst dosage on the visible light photocatalyst, we employed

the pseudo-first-order kinetic equation [64] (as depicted in Equation (4)) to fit the experimental data for the visible light photocatalytic phase.

$$\ln(C_t/C_0) = -kt \quad (4)$$

In the equation, C_0 and C_t denote the initial concentration of MB at time zero and the concentration of MB at time t, both measured in mg/L. The parameter k represents the pseudo-first-order rate constant, with units of min^{-1}, and time t is measured in minutes (min).

As shown in Figure 8, the determination coefficient (R^2) for the fit to the data consistently exceeded 70%, indicating the suitability of the pseudo-first-order model in replicating the experimental findings. Subsequently, the magnitude of the impact on visible light photocatalysis can be elucidated by comparing the fitted rate constants (k) under different conditions [46]. The rate constants associated with the varying calcination temperatures (Figure 8a), material ratios (Figure 8b), initial MB concentrations (Figure 8c), and photocatalyst quantities (Figure 8d) range from 0.009 to 0.025, 0.005 to 0.031, 0.004 to 0.033, and 0.010 to 0.026, respectively. Consequently, it is inferred that, in comparison to the calcination temperature and photocatalyst dose, the material ratios and initial MB concentrations have a more significant influence on the visible light photocatalytic performance.

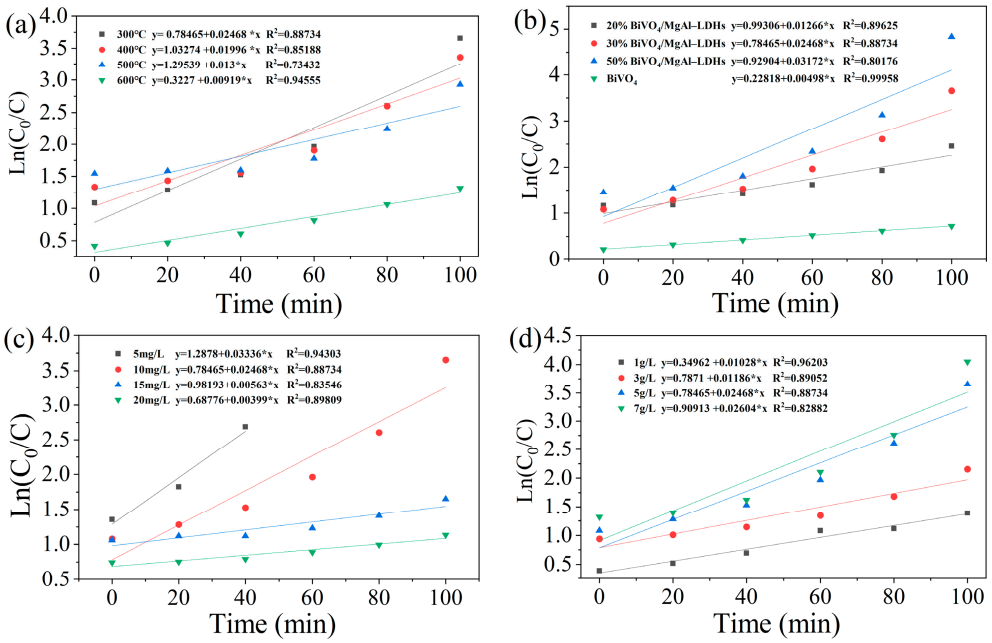

Figure 8. Kinetic fits for visible light catalytic degradation of MB in solution with different calcination temperatures (**a**), ratios (**b**), initial dye concentrations (**c**), and photo–catalyst concentrations (**d**).

3.2.6. Reusability of Photocatalysts

To evaluate the chemical stability and reusability of the composite photocatalytic material $BiVO_4$/MgAl–LDHs, after each experiment, the residue suspended in the beaker was allowed to stand for one day. Subsequently, the supernatant in the beaker was extracted, and the photocatalytic material was washed three times with absolute ethanol. Finally, the washed photocatalytic material was transferred to a dry box for drying. This process was repeated four times with the same test conditions mentioned above. As illustrated in Figure 9, after four repeated tests, the adsorption–degradation rate of MB solution can reach 88.4% (only 8.7% loss), and the results show that the newly prepared photocatalytic composite has good durability and stability. In addition, studies have shown that the repeated use of photocatalysts has little effect on their physical and chemical properties [60,65].

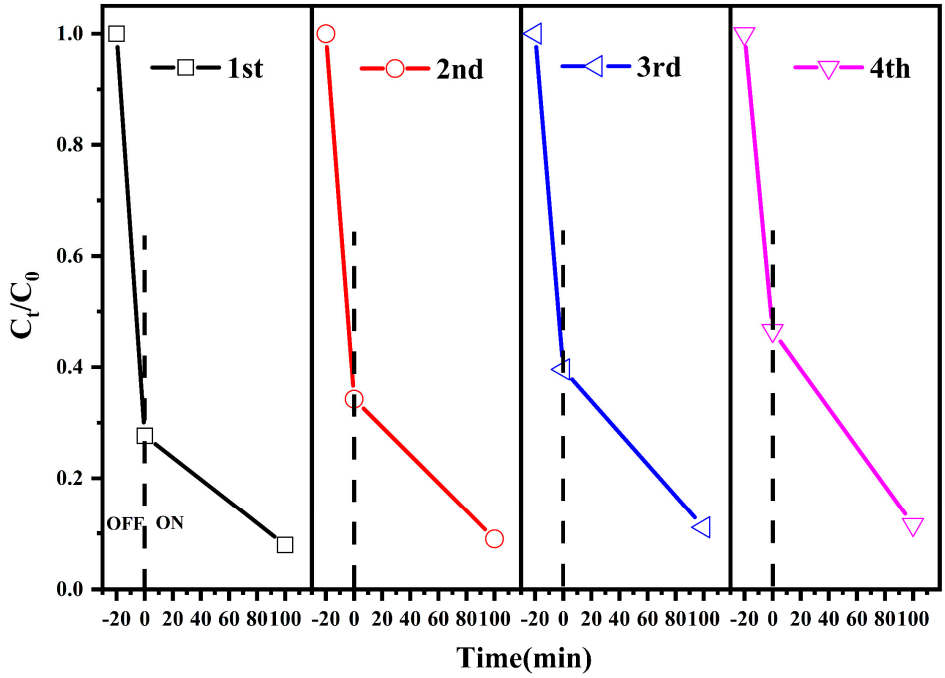

Figure 9. Cycling runs of the photocatalytic degradation of MB over the $BiVO_4$/MgAl–LDHs photocatalyst under visible light illumination.

3.3. Role of Active Species

To clarify the main active species in the photocatalytic reaction process, EDTA–2Na [66] was selected as the quencher of photogenerated holes (h^+), IPA [67] was selected as the quencher of hydroxyl radicals (·OH), and BQ [68] was used as the quencher of su–peroxide radicals ($\cdot O^{2-}$). The photocatalytic experiment was conducted under the same experimental conditions. The results are shown in Figure 10a,b. The degradation rates corresponding to EDTA-2Na, IPA, and BQ are 28%, 86%, and 34%, respectively, and the degradation rates are 64%, 6%, and 58% lower than those of the group without a quenching agent. The results show that $\cdot O_2^-$ and h^+ are the main active substances in the photocatalytic reaction process, while the effect of ·OH is relatively weak; Tang et al. drew the same conclusion [12].

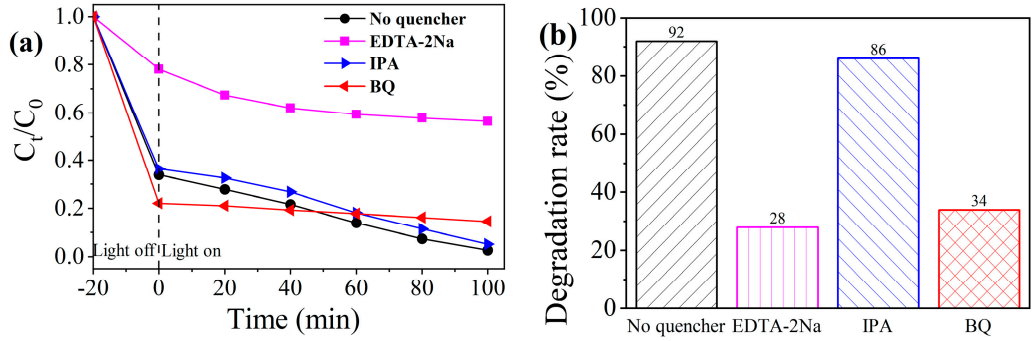

Figure 10. Relationship between the photocatalytic degradation of MB and irradiation time (**a**), as well as the MB degradation rates (**b**) with free radical scavengers.

3.4. Analysis of the Adsorption Mechanism

The study indicates that organic compounds exhibit a strong affinity for the surfaces of clay minerals [33], and as the surface area of the adsorbent increases, its adsorption capacity also increase continuously [69]. Furthermore, when MB diffuses within the composite materials with higher porosities, they are readily adsorbed onto the pore walls. From Table 1, it is evident that the composite material $BiVO_4$/MgAl–LDHs has a significantly larger specific surface area and greater porosity, providing a foundation for rapid adsorption

of a substantial quantity of MB in a short time. Moreover, the surface functional groups also play a crucial role in the adsorption process [61]. The adsorption of MB on $BiVO_4$/MgAl–LDHs in the dark is illustrated in Figure 11. The adsorption mechanism is primarily governed by the following three modes of adsorption: (i) the agglomeration of $BiVO_4$ in the composite material is ameliorated, exposing more surface active sites compared to the pure $BiVO_4$. On the other hand, the MgAl–LDHs within the composite material inherently possess large specific surface areas and abundant surface active sites. Consequently, the composite material adsorbs many MB molecules at the surface active sites. (ii) During the process of pore filling in the composite material Bi–VO_4/MgAl–LDHs, some of the MB is consumed. (iii) The free MB interacts strongly with the oxygen functional groups present in the composite material, such as OH, C–O–C, O–C=O, and forms strong π-π bonds [70] (as shown in Figure 6).

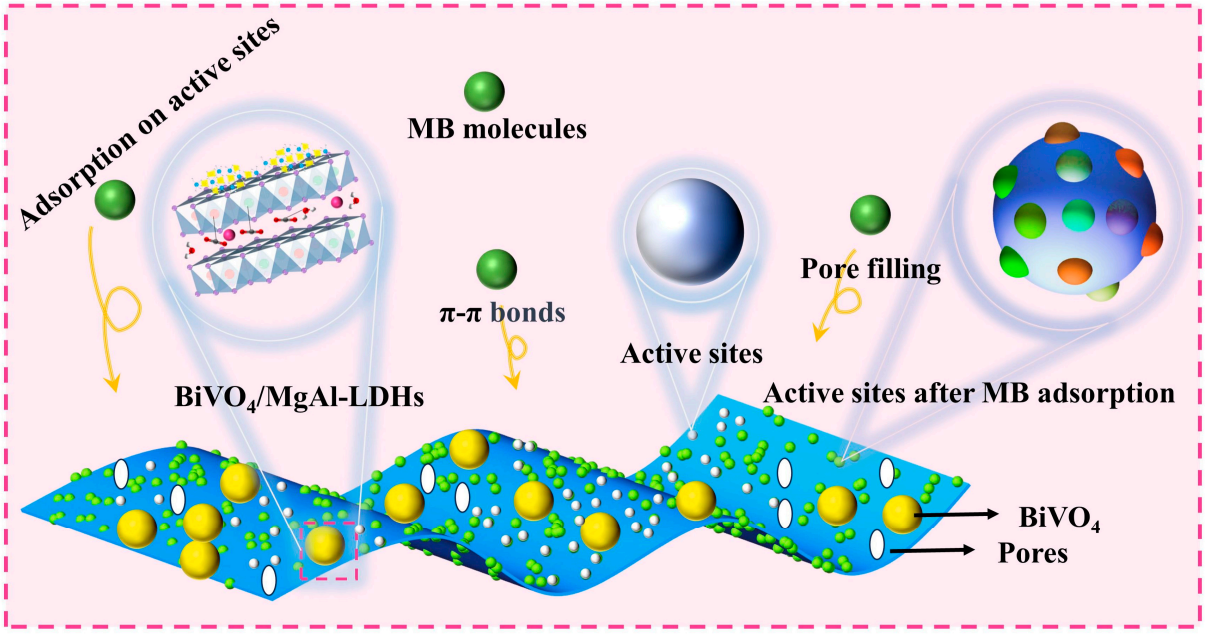

Figure 11. Adsorption of MB by $BiVO_4$/MgAl-LDHs under dark conditions.

3.5. Analysis of the Photocatalytic Mechanism

Zeng et al. [71] discovered that photocatalytic activity is primarily related to the ad–sorption capacity of the target pollutant and the degree of separation for photogenerated electron–hole pairs. Based on the aforementioned results, it is evident that the composite material $BiVO_4$/MgAl–LDHs, which was obtained by loading $BiVO_4$ during the MgAl–LDH reconstruction process, exhibits strong adsorption. The oxygen and metal vacan–cies generated during the layer-by-layer reconstruction process reduces the band gap, broadens the light absorption range, and also promotes the separation of the photogen–erated charge carriers. Additionally, research has confirmed that MgAl–LDH particles can serve as a barrier layer for electrons, leading to improved spatial charge separation [32]. As depicted in Figure 5c, compared to pure $BiVO_4$ and pure MgAl–LDHs, the com–posite material $BiVO_4$/MgAl–LDHs exhibits a smaller band gap, indicating a broader range of visible light absorption. Figure 5c shows that the band gap and valence band potential of $BiVO_4$/MgAl–LDHs are 2.06 eV and 1.35 eV, respectively. Additionally, based on the relationship between the band gap, the valence band, and the conduction band potential ($Ec = E_v - E$), the conduction band potential of $BiVO_4$/MgAl–LDHs is −0.71eV. A schematic representation of the band gap energy for $BiVO_4$/MgAl-LDHs is illustrated in Figure 12. The visible light degradation mechanism is shown in Equations (5)–(11) [60]. When the composite material $BiVO_4$/MgAl–LDHs is excited by visible light, photogener–ated electrons in the valence band are promoted to the conduction band, leaving an equal number of photogenerated

holes in the valence band. At this point, the MgAl–LDHs act as electron transfer agents, facilitating the transfer of electrons from the con–duction band to the surface of MgAl-LDHs (Equation (4)), thus reducing the rate of pho–togenerated charge carrier recombination. In the redox reactions of the photogenerated electrons and holes, O_2 is reduced to $\cdot O_2^-$ and H_2O is oxidized to ·OH. Finally, through the combined effects of various reactive species, the MB is ultimately degraded into H_2O, CO_2, and various intermediate products (Equations (8)–(11)), as illustrated in Figure 12 [24].

$$BiVO_4/MgAl - LDHs + hv \rightarrow BiVO_4(h^+) + MgAl - LDHs(e^-) \quad (5)$$

$$H_2O + h^+ \rightarrow \cdot OH \quad (6)$$

$$O_2 + e^- \rightarrow \cdot O_2^- \quad (7)$$

$$\cdot O_2^- + H_2O \rightarrow HO_2\cdot + OH^- \quad (8)$$

$$e^- + HO\cdot \rightarrow H^+ + H_2O_2 \quad (9)$$

$$e^- + H_2O_2 \rightarrow OH\cdot + OH^- \quad (10)$$

$$\cdot OH + MB \rightarrow CO_2 + H_2O + SO_4^- + NO_3^- + Cl^- \quad (11)$$

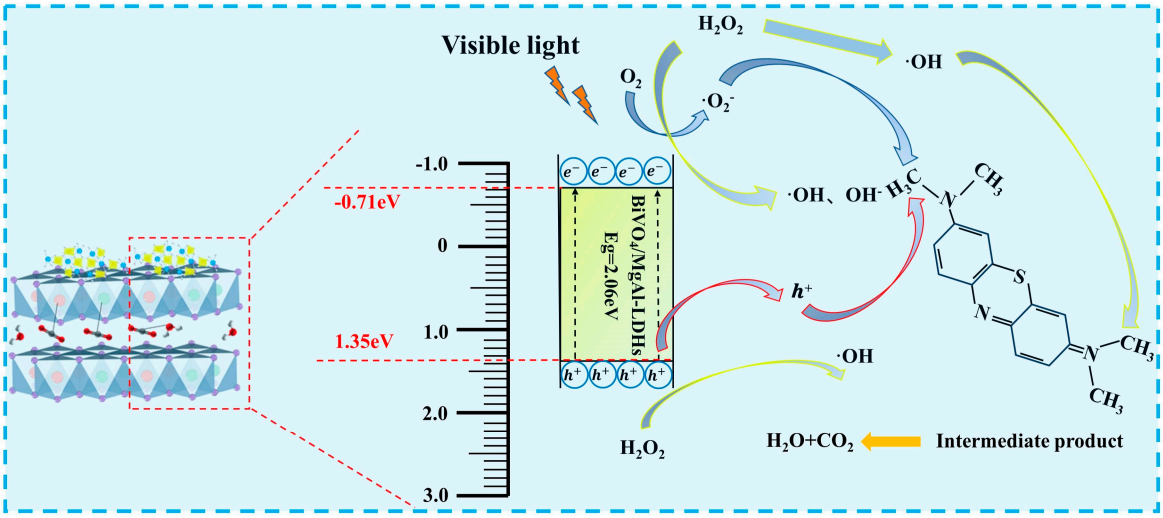

Figure 12. Schematic diagram showing the visible light catalytic degradation of MB by Bi–VO_4/MgAl–LDHs.

4. Conclusions

In this study, a high-performance, highly adsorbent photocatalytic composite material, $BiVO_4$/MgAl–LDHs, was prepared via a simple, cost–effective, and environmentally friendly method. In addition, considering the effects of calcination temperature, propor–tion, initial MB concentration, and photocatalyst dosage on the adsorption and photo–catalytic performance of the composite material, the following optimal photocatalytic conditions were obtained through continuous optimization: a calcination temperature of 300 °C, a ratio of 3:7 (the performance of the 50% $BiVO_4$/MgAl–LDHs catalyst was slightly better than that of 30% $BiVO_4$/MgAl–LDHs; considering the cost, we chose 30% Bi–VO_4/MgAl–LDHs as the preferred photocatalyst), an initial MB concentration of 10 mg/L, and a photocatalyst dosage of 5 g/L. In addition, $BiVO_4$/MgAl–LDHs showed better adsorption and photocatalytic performance than pure $BiVO_4$ and MgAl–LDHs. Under the optimal conditions, the MB adsorption rate was 66.1% in 20 min, and the amount of MB degraded during 100 min of light exposure was 92.4%. Second, the composite photocatalyst had good chemical stability and repeatable practicability, and the adsorption–degradation

rate reached 86% after four cycles. Through analyses of the adsorption mechanism and the photocatalytic mechanism of the composite material, it was revealed that the enhanced adsorption was mainly attributable to the abundant surface active sites available for adsorption, pore filling, and strong interactions with oxygen function–al groups. Furthermore, compared to pure $BiVO_4$ and pure MgAl–LDHs, the composite material $BiVO_4$/MgAl–LDHs exhibited a smaller band gap, indicating a broader visible light absorption peak. The strong adsorption capacity of the $BiVO_4$/MgAl–LDHs compo–site material enabled efficient photocatalytic degradation of MB in solution. The oxygen and metal vacancy defects generated during the layer-by-layer reconstruction process might have contributed to this, as defects can reduce the band gap and separate photo–generated charge carriers. Additionally, the MgAl–LDH particles might serve as a barrier layer for electrons and prevent recombination, thereby enhancing the spatial charge sep–aration. Finally, under the combined effects of various reactive species, the MB in solu–tion was degraded into H_2O, CO_2, and some intermediate products.

Author Contributions: Y.W.: investigation, data curation, methodology, and writing—original draft preparation. Y.X.: conceptualization, writing—review & editing, funding acquisition, and supervision. X.C.: investigation, data curation. J.W.: investigation, writing—review & editing, and supervision. All authors have read and agreed to the published version of the manuscript.

Funding: This study was supported by the Natural Science Foundation of Zhejiang Province (Grant No. LZ22E080003 for Y.X.) and the Science and Technology Project of Zhejiang Provincial Department of Transport (Grant No. 202225 for Y.X.).

Institutional Review Board Statement: Not applicable.

Informed Consent Statement: Not applicable.

Data Availability Statement: Data will be made available on request.

Conflicts of Interest: The authors declare that they have no known competing financial interest or personal relationships that could have appeared to influence the work reported in this paper.

References

1. Martínez-de La Cruz, A.; Pérez, U.M.G. Photocatalytic properties of $BiVO_4$ prepared by the co-precipitation method: Degradation of rhodamine B and possible reaction mechanisms under visible irradiation. *Mater. Res. Bull.* **2010**, *45*, 135–141. [CrossRef]
2. Tao, Y.; Ni, Q.; Wei, M.; Xia, D.; Li, X.; Xu, A. Metal-free activation of peroxymonosulfate by g-C_3N_4 under visible light irradiation for the degradation of organic dyes. *RSC Adv.* **2015**, *5*, 44128–44136. [CrossRef]
3. Zhao, Q.; Long, M.; Li, H.; Wang, L.; Bai, X.; Zhang, Y.; Li, D. Synthesis of Bi_2MoO_6 and Activating Peroxymonosulfate to Enhance Photocatalytic Activity under Visible Light Irradiation. *Cryst. Res. Technol.* **2021**, *56*, 2000219. [CrossRef]
4. Bai, R.; Yan, W.; Xiao, Y.; Wang, S.; Tian, X.; Li, J.; Xiao, X.; Lu, X.; Zhao, F. Acceleration of peroxymonosulfate decomposition by a magnetic MoS_2/$CuFe_2O_4$ heterogeneous catalyst for rapid degradation of fluoxetine. *Chem. Eng. J.* **2020**, *397*, 125501. [CrossRef]
5. Tian, N.; Huang, H.; He, Y.; Guo, Y.; Zhang, T.; Zhang, Y. Mediator-free direct Z-scheme photocatalytic system: $BiVO_4$/g-C_3N_4 organic-inorganic hybrid photocatalyst with highly efficient visible-light-induced photocatalytic activity. *Dalton Trans.* **2015**, *44*, 4297–4307. [CrossRef] [PubMed]
6. Wu, D.; Guo, J.; Wang, H.; Zhang, X.; Yang, Y.; Yang, C.; Gao, Z.; Wang, Z.; Jiang, K. Green synthesis of boron and nitrogen co-doped TiO_2 with rich B-N motifs as Lewis acid-base couples for the effective artificial CO_2 photoreduction under simulated sunlight. *J. Colloid Interface Sci.* **2021**, *585*, 95–107. [CrossRef] [PubMed]
7. Hu, Q.; Liu, Y.; Li, W.; Wang, Y.; Liao, W.; Zou, H.; Li, J.; Huang, X. Enhanced photocatalytic hydrogen evolution under visible-light using C, N co-doped mesoporous TiO_2 nanocrystals templated by ionic liquids. *Chem. Eng. J.* **2023**, *451*, 138670. [CrossRef]
8. Khan, R.; Kim, T. Preparation and application of visible-light-responsive Ni-doped and SnO_2-coupled TiO_2 nanocomposite photocatalysts. *J. Hazard. Mater.* **2009**, *163*, 1179–1184. [CrossRef] [PubMed]
9. Zhang, Z.; Lu, P.; Zhao, T.; Su, H.; Xu, Q. Improving Performance of an Integrated Solar Flow Battery by Cr- and Cu-Doped TiO_2 Photoelectrodes. *Molecules* **2023**, *28*, 171. [CrossRef] [PubMed]
10. Truppi, A.; Petronella, F.; Placido, T.; Striccoli, M.; Agostiano, A.; Curri, M.; Comparelli, R. Visible-Light-Active TiO_2-Based Hybrid Nanocatalysts for Environmental Applications. *Catalysts* **2017**, *7*, 100. [CrossRef]
11. Balati, A.; Tek, S.; Nash, K.; Shipley, H. Nanoarchitecture of TiO_2 microspheres with expanded lattice interlayers and its heterojunction to the laser modified black TiO_2 using pulsed laser ablation in liquid with improved photocatalytic performance under visible light irradiation. *J. Colloid Interface Sci.* **2019**, *541*, 234–248. [CrossRef] [PubMed]

12. Chen, F.; Yang, Q.; Wang, Y.; Zhao, J.; Wang, D.; Li, X.; Guo, Z.; Wang, H.; Deng, Y.; Niu, C.; et al. Novel ternary heterojunction photcocatalyst of Ag nanoparticles and g-C_3N_4 nanosheets co-modified $BiVO_4$ for wider spectrum visible-light photocatalytic degradation of refractory pollutant. *Appl. Catal. B Environ.* **2017**, *205*, 133–147. [CrossRef]
13. Huang, H.; He, Y.; Du, X.; Chu, P.K.; Zhang, Y. A General and Facile Approach to Heterostructured Core/Shell $BiVO_4$/BiOIp-n Junction: Room-Temperature In Situ Assembly and Highly Boosted Visible-Light Photocatalysis. *ACS Sustain. Chem. Eng.* **2015**, *3*, 3262–3273. [CrossRef]
14. Castillo, N.C.; Heel, A.; Graule, T.; Pulgarin, C. Flame-assisted synthesis of nanoscale, amorphous and crystalline, spherical $BiVO_4$ with visible-light photocatalytic activity. *Appl. Catal. B Environ.* **2010**, *95*, 335–347. [CrossRef]
15. Wang, W.; Huang, X.; Wu, S.; Zhou, Y.; Wang, L.; Shi, H.; Liang, Y.; Zou, B. Preparation of p-n junction Cu_2O/$BiVO_4$ heterogeneous nanostructures with enhanced visible-light photocatalytic activity. *Appl. Catal. B Environ.* **2013**, *134–135*, 293–301. [CrossRef]
16. Wu, J.; Chen, Y.; Pan, L.; Wang, P.; Cui, Y.; Kong, D.; Wang, L.; Zhang, X.; Zou, J. Multi-layer monoclinic $BiVO_4$ with oxygen vacancies and V^{4+} species for highly efficient visible-light photoelectrochemical applications. *Appl. Catal. B Environ.* **2018**, *221*, 187–195. [CrossRef]
17. Park, H.S.; Kweon, K.E.; Ye, H.; Paek, E.; Hwang, G.S.; Bard, A.J. Factors in the Metal Doping of $BiVO_4$ for Improved Photoelectrocatalytic Activity as Studied by Scanning Electrochemical Microscopy and First-Principles Density-Functional Calculation. *J. Phys. Chem. C* **2011**, *115*, 17870–17879. [CrossRef]
18. Zhang, X.; Quan, X.; Chen, S.; Zhang, Y. Effect of Si doping on photoelectrocatalytic decomposition of phenol of $BiVO_4$ film under visible light. *J. Hazard. Mater.* **2010**, *177*, 914–917. [CrossRef]
19. Wang, Y.; Yu, D.; Wang, W.; Gao, P.; Zhang, L.; Zhong, S.; Liu, B. The controllable synthesis of novel heterojunction CoO/$BiVO_4$ composite catalysts for enhancing visible-light photocatalytic property. *Colloids Surfaces A Physicochem. Eng. Asp.* **2019**, *578*, 123608. [CrossRef]
20. Lai, C.; Zhang, M.; Li, B.; Huang, D.; Zeng, G.; Qin, L.; Liu, X.; Yi, H.; Cheng, M.; Li, L.; et al. Fabrication of CuS/$BiVO_4$ (040) binary heterojunction photocatalysts with enhanced photocatalytic activity for Ciprofloxacin degradation and mechanism insight. *Chem. Eng. J.* **2019**, *358*, 891–902. [CrossRef]
21. Wang, T.; Li, C.; Ji, J.; Wei, Y.; Zhang, P.; Wang, S.; Fan, X.; Gong, J. Reduced Graphene Oxide (rGO)/$BiVO^4$ Composites with Maximized Interfacial Coupling for Visible Lght Photocatalysis. *ACS Sustain. Chem. Eng.* **2014**, *2*, 2253–2258. [CrossRef]
22. Wang, X.; Zhou, J.; Zhao, S.; Chen, X.; Yu, Y. Synergistic effect of adsorption and visible-light photocatalysis for organic pollutant removal over $BiVO_4$/carbon sphere nanocomposites. *Appl. Surf. Sci.* **2018**, *453*, 394–404. [CrossRef]
23. Li, Z.; Chen, M.; Ai, Z.; Wu, L.; Zhang, Q. Mechanochemical synthesis of CdS/MgAl LDH-precursor as improved visible-light driven photocatalyst for organic dye. *Appl. Clay Sci.* **2018**, *163*, 265–272. [CrossRef]
24. Qing, X.; Yuan, L.; Wang, Y.; Zhang, Z.; Bi, M.; Weng, X. Synergistic influence of Cr^{3+} and CrO_4^{2-} on the visible near-infrared spectrum of Mg-Al layered double hydroxides for efficient visible-light photocatalysis. *J. Alloys Compd.* **2021**, *872*, 159628. [CrossRef]
25. Mantilla, A.; Tzompantzi, F.; Fernández, J.L.; Góngora, J.A.I.D.; Gómez, R. Photodegradation of phenol and cresol in aqueous medium by using Zn/Al+Fe mixed oxides obtained from layered double hydroxides materials. *Catal. Today* **2010**, *150*, 353–357. [CrossRef]
26. Zhang, G.; Zhang, X.; Meng, Y.; Pan, G.; Ni, Z.; Xia, S. Layered double hydroxides-based photocatalysts and visible-light driven photodegradation of organic pollutants: A review. *Chem. Eng. J.* **2020**, *392*, 123684. [CrossRef]
27. Wang, Y.; Jing, Y.; Li, W.; Yu, M.; Ao, X.; Xie, Y.; Chen, Q. Silicate silver/flower-like magnalium hydroxide composites for enhanced visible light photodegradation activities. *RSC Adv.* **2018**, *8*, 22345–23442. [CrossRef] [PubMed]
28. Tang, H.; Zhang, W.; Meng, Y.; Xia, S. A direct Z-scheme heterojunction with boosted transportation of photogenerated charge carriers for highly efficient photodegradation of PFOA: Reaction kinetics and mechanism. *Appl. Catal. B Environ.* **2021**, *285*, 119851. [CrossRef]
29. Yang, L.; Zhao, J.; Wang, C.; Wang, Z.; Xing, C.; Guo, H.; Wang, Y.; Zhao, Z.; Hu, Z.; Cai, Z. Bi/$BiVO_4$/NiFe-LDH heterostructures with enhanced photoelectrochemical performance for streptomycin detection. *J. Environ. Sci.* **2021**, *109*, 114–122. [CrossRef] [PubMed]
30. Wu, Y.; Wang, H.; Sun, Y.; Xiao, T.; Tu, W.; Yuan, X.; Zeng, G.; Li, S.; Chew, J.W. Photogenerated charge transfer via interfacial internal electric field for significantly improved photocatalysis in direct Z-scheme oxygen-doped carbon nitrogen/CoAl-layered double hydroxide heterojunction. *Appl. Catal. B Environ.* **2018**, *227*, 530–540. [CrossRef]
31. Mortaheb, H.R.; Amini, M.H.; Sadeghian, F.; Mokhtarani, B.; Daneshyar, H. Study on a new surfactant for removal of phenol from wastewater by emulsion liquid membrane. *J. Hazard. Mater.* **2008**, *160*, 582–588. [CrossRef] [PubMed]
32. Dvininov, E.; Ignat, M.; Barvinschi, P.; Smithers, M.A.; Popovici, E. New SnO_2/MgAl-layered double hydroxide composites as photocatalysts for cationic dyes bleaching. *J. Hazard. Mater.* **2010**, *177*, 150–158. [CrossRef]
33. Yang, Z.; Wang, F.; Zhang, C.; Zeng, G.; Tan, X.; Yu, Z.; Zhong, Y.; Wang, H.; Cui, F. Utilization of LDH-based materials as potential adsorbents and photocatalysts for the decontamination of dyes wastewater: A review. *RSC Adv.* **2016**, *6*, 79415–79436. [CrossRef]
34. Carja, G.; Dartu, L.; Okada, K.; Fortunato, E. Nanoparticles of copper oxide on layered double hydroxides and the derived solid solutions as wide spectrum active nano-photocatalysts. *Chem. Eng. J.* **2013**, *222*, 60–66. [CrossRef]

35. Yuan, Z.; Bak, S.; Li, P.; Jia, Y.; Zheng, L.; Zhou, Y.; Bai, L.; Hu, E.; Yang, X.; Cai, Z.; et al. Activating Layered Double Hydroxide with Multivacancies by Memory Effect for Energy-Efficient Hydrogen Production at Neutral pH. *ACS Energy. Lett.* **2019**, *4*, 1412–1418. [CrossRef]
36. Chen, F.; Huang, G.; Yao, F.; Yang, Q.; Zheng, Y.; Zhao, Q.; Yu, H. Catalytic degradation of ciprofloxacin by a visible-light-assisted peroxymonosulfate activation system: Performance and mechanism. *Water Res.* **2020**, *173*, 115559. [CrossRef] [PubMed]
37. Hu, K.; Luo, H.; Han, Y.; Zuo, M.; Li, J. Hierarchically Porous and Magnetic $MgFe_2O_4$@MgAl-LDHs Microspheres Synthesized by a Bio-Templating Strategy for Efficient Removal of Congo Red from Water. *Chemistryselect* **2023**, *8*, e202204352. [CrossRef]
38. Li, L.; Qian, Y.; Qiao, P.; Han, H.; Zhang, H.; Giovanni, C. Preparation of LDHs Based on Bittern and Its Flame Retardant Properties in EVA/LDHs Composites. *Adv. Polym. Technol.* **2019**, *2019*, 4682164. [CrossRef]
39. Li, Y.; Dong, S.; Wang, Y.; Sun, J.; Li, Y.; Pi, Y.; Hu, L.; Sun, J. Reduced graphene oxide on a dumbbell-shaped $BiVO_4$ photocatalyst for an augmented natural sunlight photocatalytic activity. *J. Mol. Catal. A Chem.* **2014**, *387*, 138–146. [CrossRef]
40. Konstantinou, I.K.; Albanis, T.A. TiO2-assisted photocatalytic degradation of azo dyes in aqueous solution: Kinetic and mechanistic investigations: A review. *Appl. Catal. B Environ.* **2004**, *49*, 1–14. [CrossRef]
41. Yan, Y.; Liu, Q.; Wang, J.; Wei, J.; Gao, Z.; Mann, T.; Li, Z.; He, Y.; Zhang, M.; Liu, L. Single-step synthesis of layered double hydroxides ultrathin nanosheets. *J. Colloid Interface Sci.* **2012**, *371*, 15–19. [CrossRef]
42. Kang, J.; Tang, Y.; Wang, M.; Jin, C.; Liu, J.; Li, S.; Li, Z.; Zhu, J. The enhanced peroxymonosulfate-assisted photocatalytic degradation of tetracycline under visible light by g-C_3N_4/Na-$BiVO_4$ heterojunction catalyst and its mechanism. *J. Environ. Chem. Eng.* **2021**, *9*, 105524. [CrossRef]
43. Ren, Q.; Wang, G.; Wu, T.; He, X.; Wang, J.; Yang, J.; Yu, C.; Qiu, J. Calcined MgAl-Layered Double Hydroxide/Graphene Hybrids for Capacitive Deionization. *Ind. Eng. Chem. Res.* **2018**, *57*, 6417–6425. [CrossRef]
44. Yang, Y.; Zhao, S.; Bi, F.; Chen, J.; Wang, Y.; Cui, L.; Xu, J.; Zhang, X. Highly efficient photothermal catalysis of toluene over Co_3O_4/TiO_2 p-n heterojunction: The crucial roles of interface defects and band structure. *Appl. Catal. B Environ.* **2022**, *315*, 121550. [CrossRef]
45. Wang, Y.; Zhu, C.; Zuo, G.; Guo, Y.; Xiao, W.; Dai, Y.; Kong, J.; Xu, X.; Zhou, Y.; Xie, A.; et al. 0D/2D Co_3O_4/TiO_2 Z-Scheme heterojunction for boosted photocatalytic degradation and mechanism investigation. *Appl. Catal. B Environ.* **2020**, *278*, 119298. [CrossRef]
46. Zhang, L.; Meng, Y.; Dai, T.; Yao, Y.; Shen, H.; Xie, B.; Ni, Z.; Xia, S. Fabrication of a coated $BiVO_4$@LDHs Z-scheme heterojunction and photocatalytic degradation of norfloxacin. *Appl. Clay Sci.* **2022**, *219*, 106435. [CrossRef]
47. Cao, J.; Xu, B.; Lin, H.; Chen, S. Highly improved visible light photocatalytic activity of BiPO4 through fabricating a novel p–n heterojunction BiOI/$BiPO_4$ nanocomposite. *Chem. Eng. J.* **2013**, *228*, 482–488. [CrossRef]
48. She, H.; Yue, P.; Ma, X.; Huang, J.; Wang, L.; Wang, Q. Fabrication of BiVO4 photoanode cocatalyzed with NiCo-layered double hydroxide for enhanced photoactivity of water oxidation. *Appl. Catal. B Environ.* **2020**, *263*, 118280. [CrossRef]
49. Raja, A.; Rajasekaran, P.; Selvakumar, K.; Arunpandian, M.; Kaviyarasu, K.; Asath Bahadur, S.; Swaminathan, M. Visible active reduced graphene oxide-$BiVO_4$-ZnO ternary photocatalyst for efficient removal of ciprofloxacin. *Sep. Purif. Technol.* **2020**, *233*, 115996. [CrossRef]
50. Ma, X.; Liu, T.; Liu, E.; Zhang, Y. Preparation and performance of Cd-MgAl-LDHs@RGO in high efficiency electrocatalytic reduction of CO_2 to CO. *Mol. Catal.* **2023**, *535*, 112876. [CrossRef]
51. Chen, S.; Huang, D.; Zeng, G.; Xue, W.; Lei, L.; Xu, P.; Deng, R.; Li, J.; Cheng, M. In-situ synthesis of facet-dependent $BiVO_4/Ag_3PO_4$/PANI photocatalyst with enhanced visible-light-induced photocatalytic degradation performance: Synergism of interfacial coupling and hole-transfer. *Chem. Eng. J.* **2020**, *382*, 122840. [CrossRef]
52. Wang, Y.; Ding, K.; Xu, R.; Yu, D.; Wang, W.; Gao, P.; Liu, B. Fabrication of $BiVO_4/BiPO_4$/GO composite photocatalytic material for the visible light-driven degradation. *J. Clean. Prod.* **2020**, *247*, 119108. [CrossRef]
53. Zhao, W.; Feng, Y.; Huang, H.; Zhou, P.; Li, J.; Zhang, L.; Dai, B.; Xu, J.; Zhu, F.; Sheng, N.; et al. A novel Z-scheme Ag3VO4/BiVO4 heterojunction photocatalyst: Study on the excellent photocatalytic performance and photocatalytic mechanism. *Appl. Catal. B Environ.* **2019**, *245*, 448–458. [CrossRef]
54. Tao, Q.; Lin, S.; Bai, T.; Xie, J.; Dai, Y. Surface magnetized MgAl-LDHs and MgAl-LDO with excellent adsorption capacity and convenient recovery for the removal of U(VI). *J. Radioanal. Nucl. Chem.* **2023**, *332*, 325–335. [CrossRef]
55. Wang, Y.; Tan, G.; Liu, T.; Su, Y.; Ren, H.; Zhang, X.; Xia, A.; Lv, L.; Liu, Y. Photocatalytic properties of the g-C_3N_4/{010} facets BiVO4 interface Z-Scheme photocatalysts induced by $BiVO_4$ surface heterojunction. *Appl. Catal. B Environ.* **2018**, *234*, 37–49. [CrossRef]
56. Wang, F.; Wen, Z.; Zheng, Z.; Fang, W.; Chen, L.; Chen, F.; Zhang, N.; Liu, X.; Ma, R.; Chen, G. Memory Effect of MgAl Layered Double Hydroxides Promotes $LiNO_3$ Dissolution for Stable Lithium Metal Anode. *Adv. Energy Mater.* **2023**, *13*, 2203830. [CrossRef]
57. Kwon, D.; Kang, J.Y.; An, S.; Yang, I.; Jung, J.C. Tuning the base properties of Mg–Al hydrotalcite catalysts using their memory effect. *J. Energy. Chem* **2020**, *46*, 229–236. [CrossRef]
58. Takehira, K. Recent development of layered double hydroxide-derived catalysts—Rehydration, reconstitution, and supporting, aiming at commercial application. *Appl. Clay Sci.* **2017**, *136*, 112–141. [CrossRef]
59. Chen, F.; Yang, Q.; Li, X.; Zeng, G.; Wang, D.; Niu, C.; Zhao, J.; An, H.; Xie, T.; Deng, Y. Hierarchical assembly of graphene-bridged $Ag_3PO_4/Ag/BiVO_4$ (040) Z-scheme photocatalyst: An efficient, sustainable and heterogeneous catalyst with enhanced visible-

light photoactivity towards tetracycline degradation under visible light irradiation. *Appl. Catal. B Environ.* **2017**, *200*, 330–342. [CrossRef]
60. El-Hakam, S.A.; ALShorifi, F.T.; Salama, R.S.; Gamal, S.; El-Yazeed, W.S.A.; Ibrahim, A.A.; Ahmed, A.I. Application of nanostructured mesoporous silica/ bismuth vanadate composite catalysts for the degradation of methylene blue and brilliant green. *J. Mater. Res. Technol.* **2022**, *18*, 1963–1976. [CrossRef]
61. Zubair, M.; Manzar, M.S.; Mu'Azu, N.D.; Anil, I.; Blaisi, N.I.; Al-Harthi, M.A. Functionalized MgAl-layered hydroxide intercalated date-palm biochar for Enhanced Uptake of Cationic dye: Kinetics, isotherm and thermodynamic studies. *Appl. Clay Sci.* **2020**, *190*, 105587. [CrossRef]
62. Chen, F.; Yang, Q.; Niu, C.; Li, X.; Zhang, C.; Zhao, J.; Xu, Q.; Zhong, Y.; Deng, Y.; Zeng, G. Enhanced visible light photocatalytic activity and mechanism of $ZnSn(OH)_6$ nanocubes modified with AgI nanoparticles. *Catal. Commun.* **2016**, *73*, 1–6. [CrossRef]
63. Zhang, Y.; Sun, A.; Xiong, M.; Macharia, D.K.; Liu, J.; Chen, Z.; Li, M.; Zhang, L. TiO_2/BiOI p-n junction-decorated carbon fibers as weavable photocatalyst with UV-vis photoresponsive for efficiently degrading various pollutants. *Chem. Eng. J.* **2021**, *415*, 129019. [CrossRef]
64. Xia, S.; Zhang, G.; Meng, Y.; Yang, C.; Ni, Z.; Hu, J. Kinetic and mechanistic analysis for the photodegradation of gaseous formaldehyde by core-shell CeO_2@LDHs. *Appl. Catal. B Environ.* **2020**, *278*, 119266. [CrossRef]
65. Afzal, M.Z.; Zu, P.; Zhang, C.; Guan, J.; Song, C.; Sun, X.; Wang, S. Sonocatalytic degradation of ciprofloxacin using hydrogel beads of TiO_2 incorporated biochar and chitosan. *J. Hazard. Mater.* **2022**, *434*, 128879. [CrossRef]
66. Geng, K.; Wu, Y.; Jiang, G.; Liu, K.; Jiang, L. RuC@g-C_3N_4(H+)/TiO_2 visible active photocatalyst: Facile fabrication and Z-scheme carrier transfer mechanism. *Mol. Catal.* **2018**, *458*, 33–42. [CrossRef]
67. Manikandan, S.; Sasikumar, D.; Maadeswaran, P. Synthesis, structural and optical properties of phosphorus doped MnO_2 nanorods as an under sunlight illumination with intensify photocatalytic for the degradation of organic dyes. *Optik* **2022**, *261*, 169185. [CrossRef]
68. Ju, P.; Wang, P.; Li, B.; Fan, H.; Ai, S.; Zhang, D.; Wang, Y. A novel calcined Bi_2WO_6/$BiVO_4$ heterojunction photocatalyst with highly enhanced photocatalytic activity. *Chem. Eng. J.* **2014**, *236*, 430–437. [CrossRef]
69. Orthman, J.; Zhu, H.Y.; Lu, G.Q. Use of anion clay hydrotalcite to remove coloured organics from aqueous solutions. *Sep. Purif. Technol.* **2003**, *31*, 53–59. [CrossRef]
70. Fan, S.; Wang, Y.; Wang, Z.; Tang, J.; Tang, J.; Li, X. Removal of methylene blue from aqueous solution by sewage sludge-derived biochar: Adsorption kinetics, equilibrium, thermodynamics and mechanism. *J. Environ. Chem. Eng.* **2017**, *5*, 601–611. [CrossRef]
71. Zeng, B.; Chen, X.; Chen, C.; Ning, X.; Deng, W. Reduced graphene oxides loaded-ZnS/CuS heteronanostructures as high-activity visible-light-driven photocatalysts. *J. Alloys Compd.* **2014**, *582*, 774–779. [CrossRef]

Disclaimer/Publisher's Note: The statements, opinions and data contained in all publications are solely those of the individual author(s) and contributor(s) and not of MDPI and/or the editor(s). MDPI and/or the editor(s) disclaim responsibility for any injury to people or property resulting from any ideas, methods, instructions or products referred to in the content.